JOURNAL OF GEOPHYSICAL RESEARCH, VOL. 96, NO. C3, PAGES 4605–4621, MARCH 15, 1991

Wave Propagation in the Marginal Ice Zone: Model Predictions and Comparisons With Buoy and Synthetic Aperture Radar Data

ANTONY K. LIU

Oceans and Ice Branch, NASA Goddard Space Flight Center, Greenbelt, Maryland

BENJAMIN HOLT

Jet Propulsion Laboratory, California Institute of Technology, Pasadena

PARIS W. VACHON

Canada Centre for Remote Sensing, Ottawa

In this paper the ocean wave dispersion relation and viscous attenuation by a sea ice cover are studied for waves propagating into the marginal ice zone (MIZ). The derivation of the dispersion relation and the viscous attenuation by an ice sheet are discussed for waves under flexure and pack compression. In the MIZ, the flexure effect is important for short waves. For a fixed wave period the changes in wavelength and group velocity as a function of ice thickness are significant. In turn, the exponential wave attenuation rate shows a rollover at short wave periods, whereby the rapid increase in wave attenuation rate with decreasing wave period slows down or even turns into a decrease. The Labrador Ice Margin Experiment (LIMEX), conducted on the MIZ off the east coast of Newfoundland, Canada, in March 1987, provides us with aircraft synthetic aperture radar (SAR) imagery, wave buoy, and ice property data. On the basis of the wave number spectrum from the SAR data and the concurrent wave frequency spectrum from the ocean buoy data and accelerometer data on the ice during LIMEX '87, the dispersion relation has been estimated and compared with a model. Wave energy attenuation rates are estimated from SAR data and the ice motion package data which were deployed at the ice edge and into the ice pack, and compared with the model. The model-data comparisons are reasonably good for the ice conditions observed during LIMEX '87. Some previously reported data of wave attenuation in the MIZ are revisited for model comparison.

1. INTRODUCTION

Ocean surface waves from the open sea may penetrate into the marginal ice zone and contribute to the breakup of floes and to other processes that modify the ice cover. Ice conditions are generally not uniform within the marginal ice zone (MIZ). Here strong mesoscale air-ice-sea interactive processes occur which control the advance and retreat of the ice margin. Variability in ice conditions may be sufficient to change the wave dispersion relationship. When a train of ocean waves enters the MIZ, the wave energy is progressively attenuated with increasing penetration into the ice field. Most of the previous efforts to study wave-ice interactions in the MIZ have been focused on wave propagation and dissipation as reported by *Wadhams* [1973, 1975], *Martin and Kauffman* [1981], and *Wadhams et al.* [1986]. They found an exponential decay in wave amplitude with distance from the ice edge.

During the Labrador Ice Margin Experiment in 1987 (LIMEX '87), the ice off Newfoundland was heavily compacted against the coast and was composed of floes, for the most part smaller than 20 m in diameter, in a matrix of brash ice which were often heavily rafted to greater than 1 m in thickness. An overview of LIMEX '87 ice observations has been reported by *Carsey et al.* [1989]. Swell from the open ocean penetrated into the ice pack to distances of 5–150 km.

Paper number 90JC02267.
0148-0227/91/90JC-02267$05.00

The extensive rafting was evidence of a combination of high ice stress and large-amplitude swell; models of rafting indicate that bending moment stresses would generate cakes of this size as reported by *Shen et al.* [1987]. No rafting was observed to have taken place during the experiment and the event must have taken place earlier in the season.

Swell penetration was observed in the aircraft synthetic aperture radar (SAR) images in the MIZ but was barely visible on coincident aerial photographs. SAR imaging of waves in ice has previously been considered by *Dawe and Parashar* [1978] and by *Raney* [1981]. *Lyzenga et al.* [1985] suggested that velocity bunching is the dominant image contrast modulation mechanism for these waves that enables the SAR imaging of waves in ice. Further study on this subject has been reported by *Raney et al.* [1988, 1989]. Finally, ice motion sensor packages were deployed on ice floes in the MIZ during LIMEX '87 as reported by *Eid et al.* [1989] which provide wave frequency spectra.

The highly compact ice situation has recently been modeled by *Liu and Mollo-Christensen* [1988] to study wave propagation in a solid pack on the basis of observations in the Weddell Sea. They have developed models for wave refraction at the ice edge, the effects of an ice pack on wave dispersion, and viscous damping. The theory of flexural gravity waves has been used by *Wadhams* [1973] and *Squire* [1984]; in their studies the wave energy is coupled between the water and an ice layer on top. The cracking of sea ice due to flexure by incoming swell is the primary cause of ice breakup. In regions exposed to constant wave action, such as the Labrador Sea, any sizable floe will be reduced to 10-m ice cakes after a few hours of wave activity [*Squire and Allan*, 1980]. During periods of quiescence and low temperatures, the debris is refrozen into composite floes, only to be broken again by the onset of further wave action. The spectral evolution of wind-generated surface waves in a dispersed ice field has been studied by *Masson and LeBlond* [1989].

Wadhams et al. [1988] reported the attenuation rates of ocean waves in the MIZ based on the results of a series of field experiments carried out between 1978 and 1983 in the Greenland and Bering seas. They found that the decay of waves is exponential, with a decay coefficient which generally increases with frequency except for a rollover at higher frequencies. The model of wave scattering by *Wadhams* [1975] and the model of viscous fluid by *Weber* [1987] do not predict the rollover effect. The viscous damping model developed by *Liu and Mollo-Christensen* [1988] predicts the rollover at high frequencies due to the change in wave dispersion caused by ice conditions.

In this paper, the model of wave propagation in the MIZ which includes wave dispersion and viscous attenuation are presented in section 2. Section 3 describes LIMEX '87 ice surface measurements and wave buoy data. The SAR data analysis and procedure are outlined in section 4. Model-data comparisons and results are presented in section 5 with the revisit of *Wadhams*' [1988] data, followed by a discussion in section 6.

2. Model of Wave Propagation

A summary of the wave propagation model is presented here, with a more detailed presentation given by *Liu and Mollo-Christensen* [1988], who derive the dispersion relation and viscous attenuation rate for waves under pack compression. However, in the MIZ the compressive stress is relatively negligible. Considering the ice to be a thin elastic plate of thickness h on top of water with finite depth H, the dispersion relation for a flexural-gravity wave of frequency ω and wave number k is given by [*Wadhams*, 1973]

$$\omega^2(k) = \left[gk + \frac{Eh^3k^5}{12(1-s^2)\rho_w}\right] \Big/ \left(\coth kh + \frac{\rho_i hk}{\rho_w}\right)$$
$$= (gk + Bk^5)/(1 + kM) \quad (1)$$

where E is Young's modulus of elasticity (for ice, $E = 6 \times 10^9$ N m^{-2}), s is Poisson's ratio (for ice, $s = 0.3$), and g is the acceleration of gravity. The density of sea ice is approximately $\rho_i = 0.9\ \rho_w$, where the density of seawater is approximately $\rho_w = 1025$ kg m^{-3}. The coefficients B and M denote the effects that modify the frequency due to bending and the inertia of the ice respectively. For deep water, $kH \gg 1$. Equation (1) reduces to and agrees with the no compressive stress result of *Liu and Mollo-Christensen* [1988].

Since wave energy propagates at group velocity, group velocity plays a fundamental role in wave propagation and dissipation. For deep water, $kH \gg 1$, the group velocity is

$$C_g = \frac{\partial \omega}{\partial k}$$
$$= [g + (5 + 4kM)Bk^4]/[2\omega(1 + kM)^2] \quad (2)$$

Note that when $B = M = 0$, (1) and (2) reduce to the open water wave dispersion relation.

The theories that have been presented to explain wave dissipation in ice include wave scattering by individual ice floes [*Wadhams*, 1975], inelastic bending of the ice sheet [*Wadhams*, 1973], and the effects of a viscous ice layer [*Weber*, 1987]. *Liu and Mollo-Christensen* [1988] have developed a viscous boundary layer model for wave attenuation in the MIZ. When the ice is highly compact with high concentration, the flexural waves obey the dispersion relation (1) as similar waves in a continuous ice sheet. The wave energy attenuation rate is

$$\alpha = \frac{\sqrt{\nu}\, k \sqrt{\omega}}{C_g \sqrt{2}\,(1 + kM)} \quad (3)$$

where the group velocity c_g is given by (2) and ν is the eddy viscosity in the turbulent boundary layer beneath the ice. The eddy viscosity is not a physical parameter but a phenomenological one that can be determined only as a function of the flow conditions. Flow conditions in the turbulent boundary layer are determined by ice thickness, floe size, ice concentration, and wavelength. For the ocean, estimates of ν ranging from 1 cm^2 s^{-1} to 10^3 cm^2 s^{-1} have been put forward. In the Arctic Ocean, the eddy viscosity was estimated by *Brennecke* [1921] to be 160 cm^2 s^{-1} under the ice, and by *Hunkins* [1966] to be 24 cm^2 s^{-1} from ice drift. In the MIZ, the eddy viscosity is highly variable and depends on the roughness of the underside of the ice cover.

3. LIMEX '87 Surface Measurements

The field experiment took place during the last 2 weeks in March 1987 off the southeast coast of Newfoundland at various locations in relation to the coast and ice pack [*Carsey et al.*, 1989]. Figure 1 indicates the ship position for both March 23 and 26 at the time of aircraft overflights. Also shown are the single-frame SAR image locations, which are subsets of extensive areal mosaics flown on those 2 days, with indicated flight and look directions. The ice edges were determined from the areal SAR image mosaics. For the wave dispersion study, the SAR wave analysis was performed on images A–E with the wave spectra obtained within the first 2 km inside the ice edge. Note that frames D and E are located over fairly shallow bathymetric features. For the wave attenuation study, SAR frames A, E, F, and G were analyzed with the wave spectra obtained along a continuous swath from the ice edge 6 km and 28 km, respectively, into the ice cover. The analysis for image A extended toward the coast to water depths that are greater than 90 m and the waves are considered to be deepwater waves unaffected by shallow water.

The ice conditions during the experiment are summarized by *Carsey et al.* [1989] and *Drinkwater* [1989]. The ice floes were generally smaller than 20 m in diameter, highly rafted, and contained in a compacted matrix of brash ice due to southeasterly winds. The ice was almost entirely present in 10/10 ice concentration. The small floe size and presence of rafting are indicative of exposure of first-year ice to large surface waves. On March 21 the brash ice between the floes was frozen, resulting in large composite floes. During this period the occurrence of swell from the north and east entering the ice pack, in concert with increasing tempera-

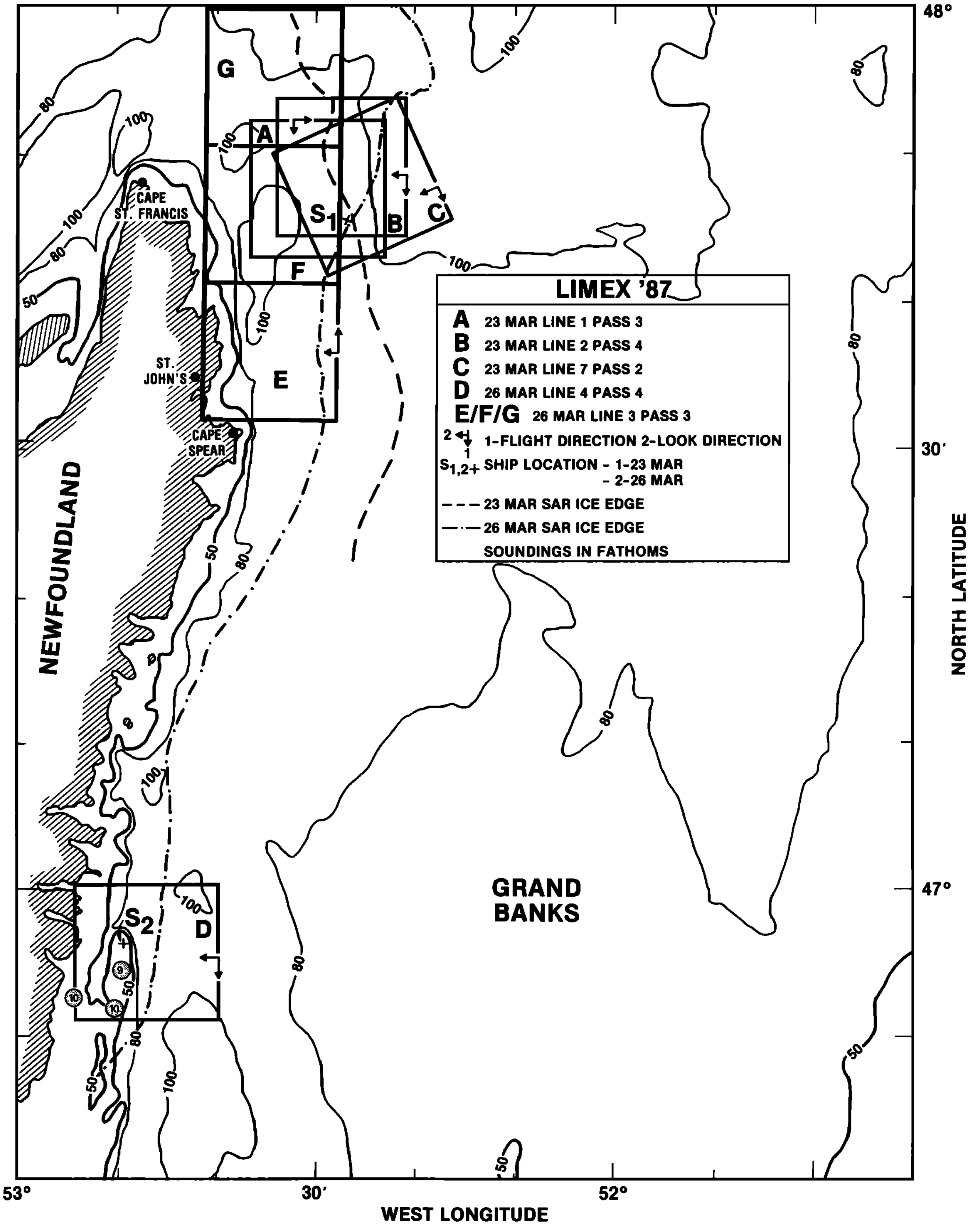

Fig. 1. Bathymetric map of the area off Newfoundland indicating the location of SAR images used in wave analysis and of the research ship at time of SAR data acquisition. The ice edge was derived from SAR areal mosaics.

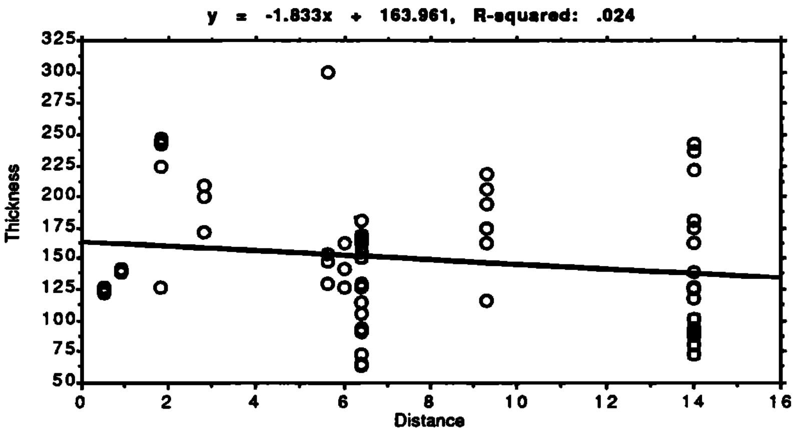

Fig. 2. Measurements of ice thickness for entire experiment relative to distance from approximate ice edge. On some floes, multiple measurements of thickness were obtained and each measurement is represented as an individual point.

tures near or above 0°C, resulted in the brash ice becoming unconsolidated between the floes, actually being ground into granular ice which remained unfrozen. From the SAR image mosaics, the swell was visible within the ice pack predominantly in areas of small floes and unconsolidated brash as determined from surface observations. The visible limit of swell penetration progressed into the pack an average of 10 km d^{-1} in relation to the ice edge from March 21 to 26.

The ice studied consisted entirely of first-year ice, as determined by salinity profiles [*Drinkwater*, 1989]. The thickness measurements are shown in Figure 2 in relation to the estimated position of the measurement from the ice edge. The mean ice thickness for all floes measured was 1.5 m. For undeformed ice, the thickness measurements were from 0.8 to 1.0 m, which is estimated to be the thermodynamic growth for one season in this region [*Carsey et al.*, 1989]. Thus much of the thicker ice measurements are a result of single and even multiple rafting, especially in the measurements greater than 2.0 m. While the correlation between thickness and distance is negligible (0.156), there appears to be a more uniform and broader distribution of ice thickness with increasing distance into the ice pack, with more random measurements nearer the ice edge. This difference near the edge is most likely due to difficulties in sampling, since there was decreased physical access and mobility between floes at the ice edge caused by an increase of brash between the floes.

Floe sizes measured from the surface are plotted by distance from the ice edge in Figure 3. The mean floe size is about 11.5 m. The correlation between size and distance from the edge is slightly larger (0.253) than that of ice thickness, but again these measurements are highly biased toward larger-sized floes on account of physical access and mobility, as was mentioned above. Floe sizes determined from helicopter aerial photography indicate a range of mean floe sizes of about 7 m within 2 km of the ice edge increasing to between 10 and 18 m towards the coast with the maximum floe sizes between 20 and 50 m [*Eid et al.*, 1989].

Surface wave measurements were made during the field experiment using a Delft wave buoy (W. Thomas, personal communication, 1988) and several wave accelerometers [*Eid et al.*, 1989]. The wave buoy is easily deployed and provides nondirectional wave spectra as derived from vertical acceleration (heave) measured continuously. The wave accelerometer is a package placed on an ice floe which measures linear acceleration along three orthogonal axes and pitch and roll, and the data may be processed to produce directional wave spectra. However, since the motion of the ice floe itself where the package is placed is not known, it is not possible to directly relate the axes measurements to wave slope and

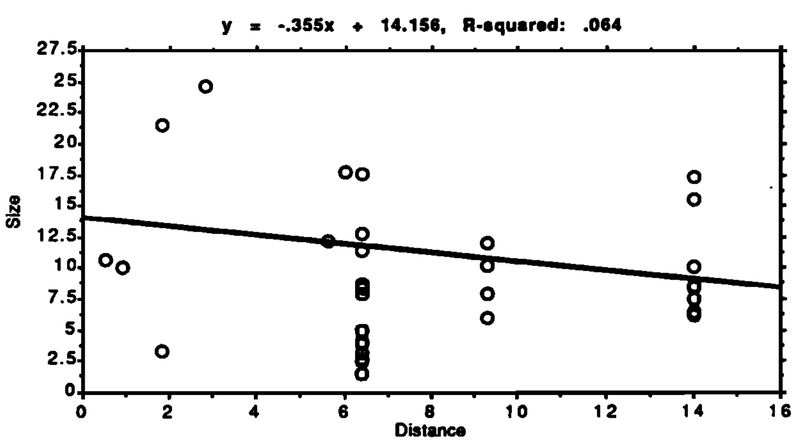

Fig. 3. Surface measurements of floe size for entire experiment relative to distance from approximate ice edge.

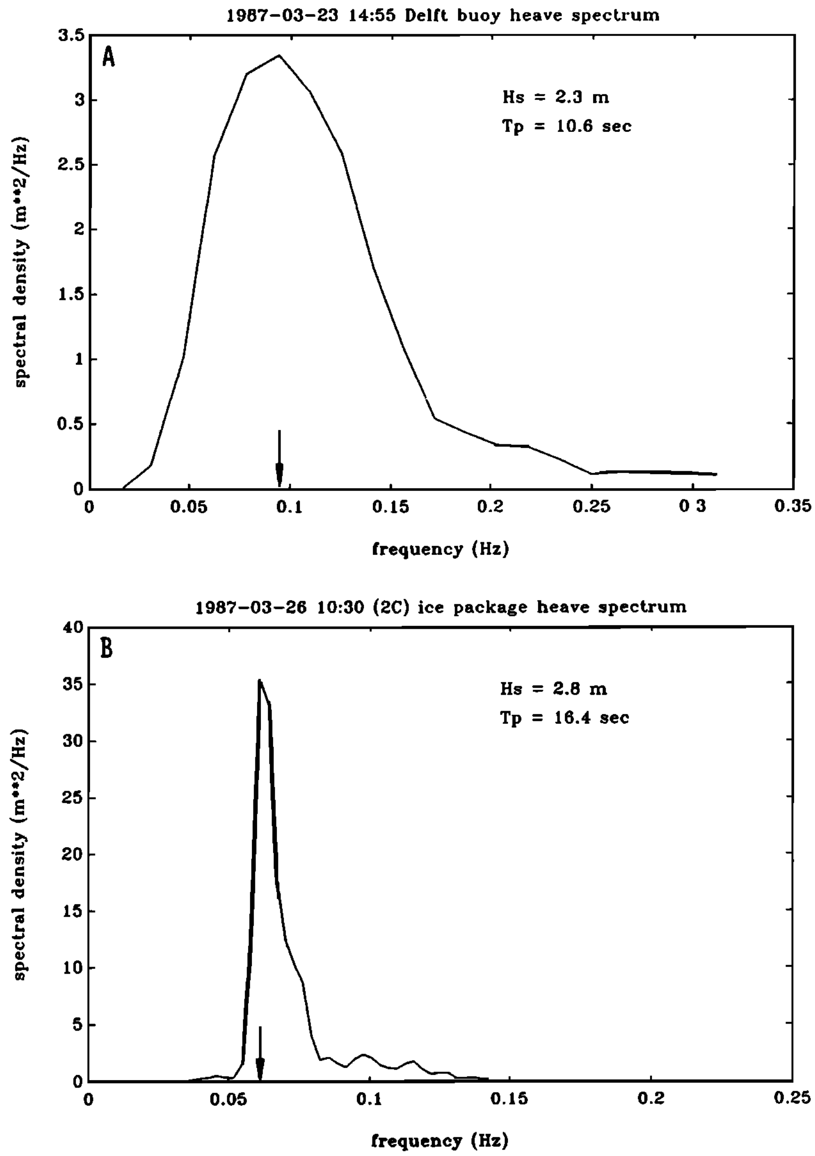

Fig. 4. Wave spectra from (*a*) Delft wave buoy for March 23, and (*b*) ice motion package for March 26.

elevation except to assume that the relatively small floes (10 m) follow the generally longer wavelength swell (greater than 150 m) fairly closely. To reduce the uncertainty in floe motion with waves, only heave measurements have been utilized in this study, since they are relatively independent of ice floe shape and size.

For the wave dispersion study, the following wave buoy data were utilized. For March 23, only the wave frequency spectra from the Delft buoy were available as shown in Figure 4*a*. Two measurements occurred on that day at 1455 UT and 1525 UT, within 75 and 45 min respectively, of the SAR data, in open water 3 km and 0.6 km, respectively, east of the ice edge. The measured dominant peak wave periods of 9.2 and 10.6 s have been averaged (9.9 s) for comparison with the model results. For March 26, only the wave frequency spectra from the wave accelerometers on ice were obtained. Three measurements were made within 5 hours of the SAR data acquisition time at nearly the same distance of 0.5 km from the ice edge. The heave spectrum for the measurement closest in time to the SAR data is shown in Figure 4*b*. The measured dominant peak wave periods of 14.8, 16.4, and 17.1 s result in an average of 16.1 s which is used for comparison with the model results.

For the wave attenuation study, ice motion package data from March 25 were utilized. One motion package was deployed on a floe 0.5 km from the ice edge and acquired data for 5.5 hours. Wave periods measured from this package ranged from 8.7 to 10.0 s. Another package was placed on floes which were at distances of 1.5, 2.8, and 4.3 km from the edge and measured peak wave periods of 8.7, 9.5, and 18.0 s, respectively.

4. SAR DATA ANALYSIS

The Canada Centre for Remote Sensing (CCRS) Convair 580 C-band SAR system was flown operationally for the first time during LIMEX '87. The CCRS SAR is a digitally controlled radar system which employs a platform motion compensation system. The imagery used in this study was processed on board by a real-time SAR processor. A complete description of the radar system and its properties is given by *Livingstone et al.* [1987].

Five frames of SAR image data for the wave dispersion study have been utilized as shown by frames A, B, C, D, and E in Figure 1. All data were collected in the "narrow swath" mode (incidence angles of >45°), with *HH* (horizontal transmit/horizontal receive) polarization, and used a land model sensitivity time control (STC) received power weighting function. The real-time processor provides imagery with seven looks (with looks summed in amplitude). The focus is fixed for a static target model. The images were interpolated postflight to 3.9 by 3.9 m pixels; the swath width is 18 km.

In this work, SAR image data of waves in the marginal ice zone from two separate days are considered: March 23, 1987, and March 26, 1987 (Figure 1). The ocean wave conditions were substantially different on these particular days, as referenced by the Delft buoy spectra and the wave-induced ice motion sensor package spectra. For March 23, three nominally overlapping passes with scenes from separate flight lines are used as shown by frames A, B, and C in Figure 1. The March 23 data sets are shown in Figure 5. For March 26, two passes over two separate locations further south in the ice pack are used as shown by frames D, and E in Figure 1. The March 26 data sets are shown in Figure 6. For the wave attenuation study, three images taken March 26 located north of Cape St. Francis are used as shown by frames E, F, and G in Figure 1.

Analyses of the SAR imagery are given by *Carsey et al.* [1989] and *Drinkwater* [1989] and a brief summary is given here. The radar return from the sea ice in this region is due to extreme surface roughness and wetted surface conditions. The ice is extremely rough owing to rafting resulting from wave-ice interaction. The many small floes and high concentration of interfloe brash ice within the outermost ice pack produces a bright radar backscatter return since the edges of floes and rafted blocks act as corner reflectors to the radar. Nearer the coast, the floes are larger and flatter and the radar return is reduced. The air temperatures during this study period were often above 0°C, which reduces both the backscatter return and contrast on an individual floe because of the wetted snow cover and surface ponding. The combination of floes close in size to the SAR resolution and the wetted surface conditions results in reduced detectability of separate floes and surface features in the outermost ice margin. The narrow bright lines near the ice edge are regions of varying concentrations of brash ice and floes. In Figure 6*a* the line of sharp contrast in the middle of the image represents the demarcation of a shear zone where ice on the eastern portion of the pack has become more broken up by waves and has moved faster with respect to the westernmost ice, where the floes have remained larger and held fast to the coast at least in a relative sense to the outermost ice [*Drinkwater and Squire*, 1989].

Waves are imaged as periodic modulations in the ice cover, as can be seen clearly seen in Figure 5, which appears bright in contrast to the darkly appearing open water. This zone is composed of small ice floes separated by brash ice. Note that in Figure 5*b*, a periodic displacement of the ice-water boundary is apparently due to the velocity bunching effects associated with the azimuthally traveling wave orbital motion [*Lyzenga et al.*, 1985]. The waves in Figure 6 are seen propagating nearly all the way to the coastline. For waves in ice, the MIZ acts like a low-pass filter owing to wave refraction at ice edge and wave attenuation, effectively suppressing the high-frequency wave components. The absence of high-frequency waves, in turn, lengthens the coherence time and acts to enhance wave visibility in ice imagery via velocity bunching. It is generally accepted that the dominant mechanism which allows a SAR to image azimuthally traveling waves in ice is velocity bunching [*Lyzenga et al.*, 1985]; a natural consequence of coherently sensing scatterer motions at the wave orbital velocity. For range-traveling waves in ice, the tilt modulation contribution should be the dominant mechanism of SAR imaging.

From each pass, subscenes approximately 2 km on each side (512 by 512 pixels) have been extracted which are subjected to a spectral analysis procedure. For the analysis of dispersion five subscenes extracted from each image were considered. The subscenes were uniformly spaced across the image data set, with the center of each subscene located approximately 2 km from the ice edge. For the attenuation analysis, a series of subscenes were selected that extended into the ice cover as far as the waves were visible.

The spectral analysis procedure consisted of squaring, trend removal, Cosine taper windowing, two-dimensional fast Fourier transform (FFT), amplitude detection, normalization by the subscene mean, smoothing, and scanning distortion correction. The analysis procedures are discussed further by *Vachon et al.* [1988] and in *Raney et al.* [1989]. Scanning distortion is an along-track scale distortion which results when a scanning sensor, such as a SAR, collects imagery of an object moving in the direction of flight. The scanning distortion correction was performed for both the case of the deep water, open ocean dispersion relation, and for the case of a 1.5-m ice thickness according to the waves-in-ice model of *Liu and Mollo-Christensen* [1988]. Since there were no significant differences for peak long waves, the open water dispersion relation was used for the scanning distortion correction.

Figure 7 shows representative imagery and scanning distortion corrected spectra from each of the 2 days considered. The subscenes from March 23, line 1, pass 3, are located at increasing range on the ground from the radar (Figure 5*b*). The peak wavelength and propagation direction are given in Table 1 as a function of radar slant range from the airplane nadir track. There is no significant trend or tendency for the waves to shift toward a more range-traveling direction in these results. Therefore issues such as coherence time limitations are not important for SAR measurement of waves in ice [*Raney*, 1981].

Quantitative peak locations in terms of representative wavelength and direction are given in Table 2 for the uncorrected spectrum and the two cases of scanning distortion correction. It is not obvious that the second peak considered is representative of a true secondary ocean wave mode. It may simply be a consequence of velocity bunching nonlinearities, as described by *Raney and Vachon* [1988]. The longer waves are essentially insensitive to which dispersion relation is used for the scanning distortion correction.

Based upon the scanning distortion corrected peak spectral values, it is concluded that the (average) primary wavelength in the marginal ice zone at the time of the SAR data collections was 228 ± −15 m on March 23 and 310 ± −29 m on March 26. These wavelength values will be used in subsequent comparisons with theoretical dispersion relations.

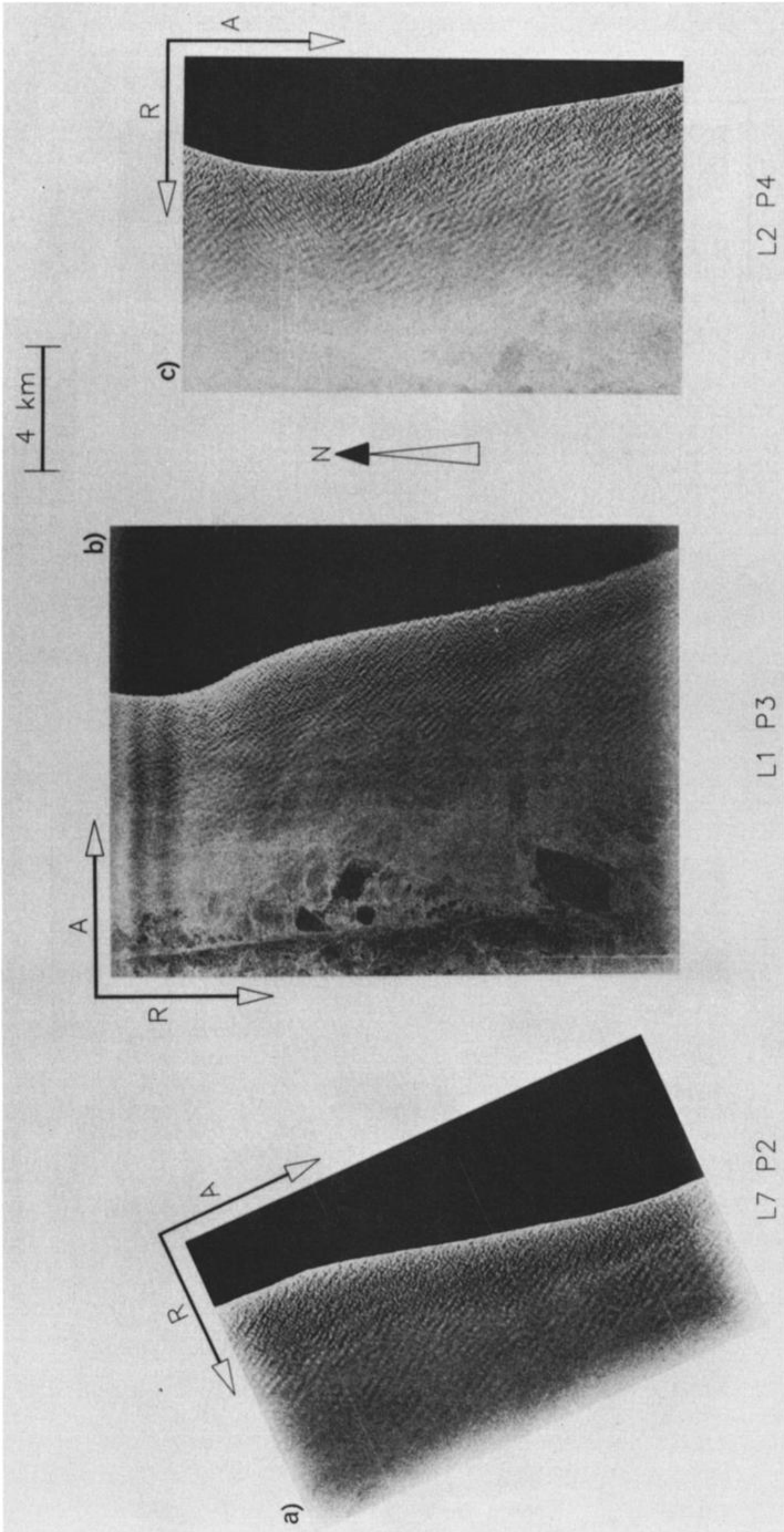

Fig. 5. SAR image scenes considered from March 23, 1987, for wave dispersion analysis: (*a*) line 7, pass 2; (*b*) line 1, pass 3; (*c*) line 2, pass 4.

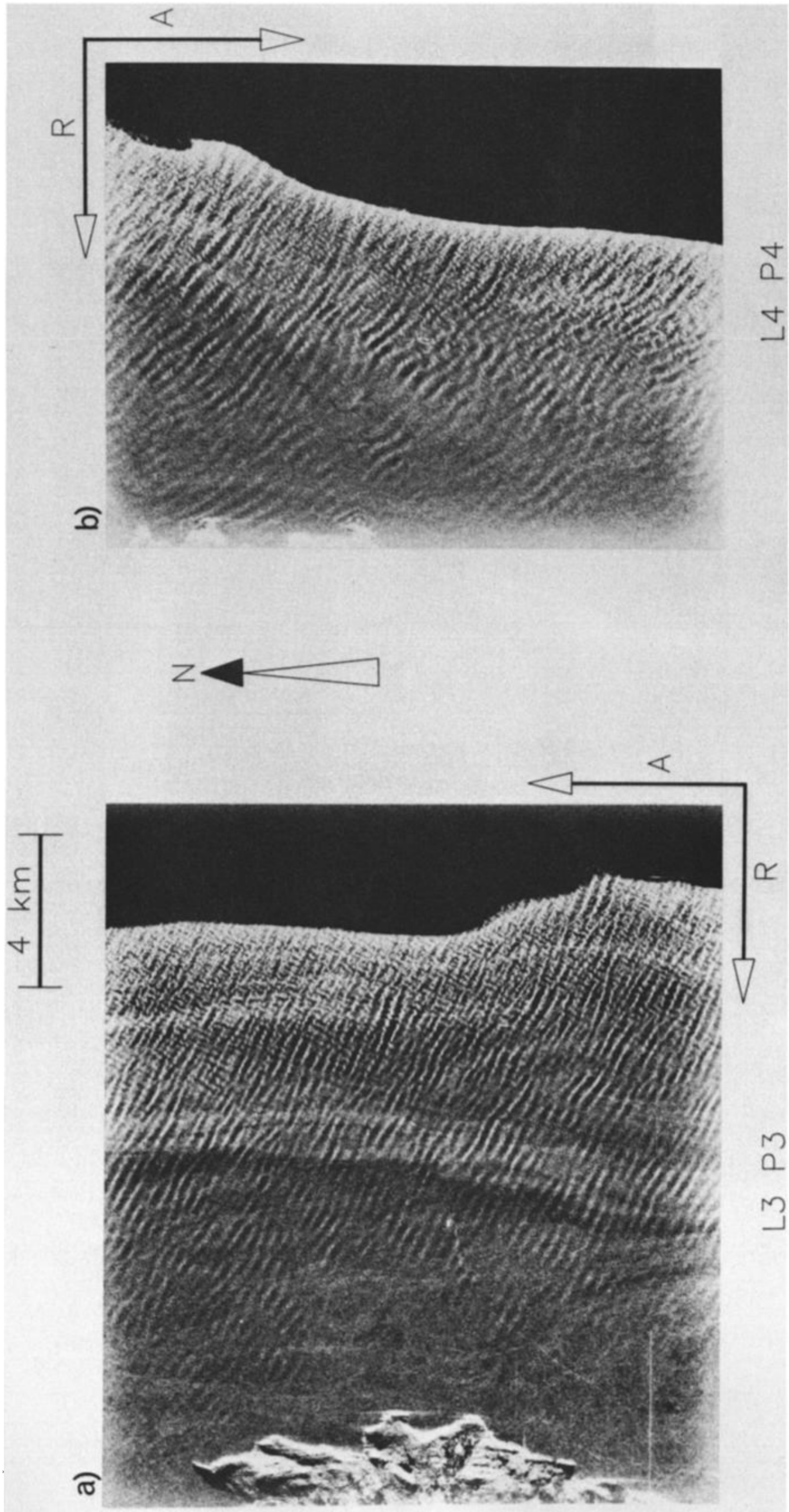

Fig. 6. SAR image scenes considered from March 26, 1987, for wave dispersion analysis: (*a*) line 3, pass 3; (*b*) line 4, pass 4.

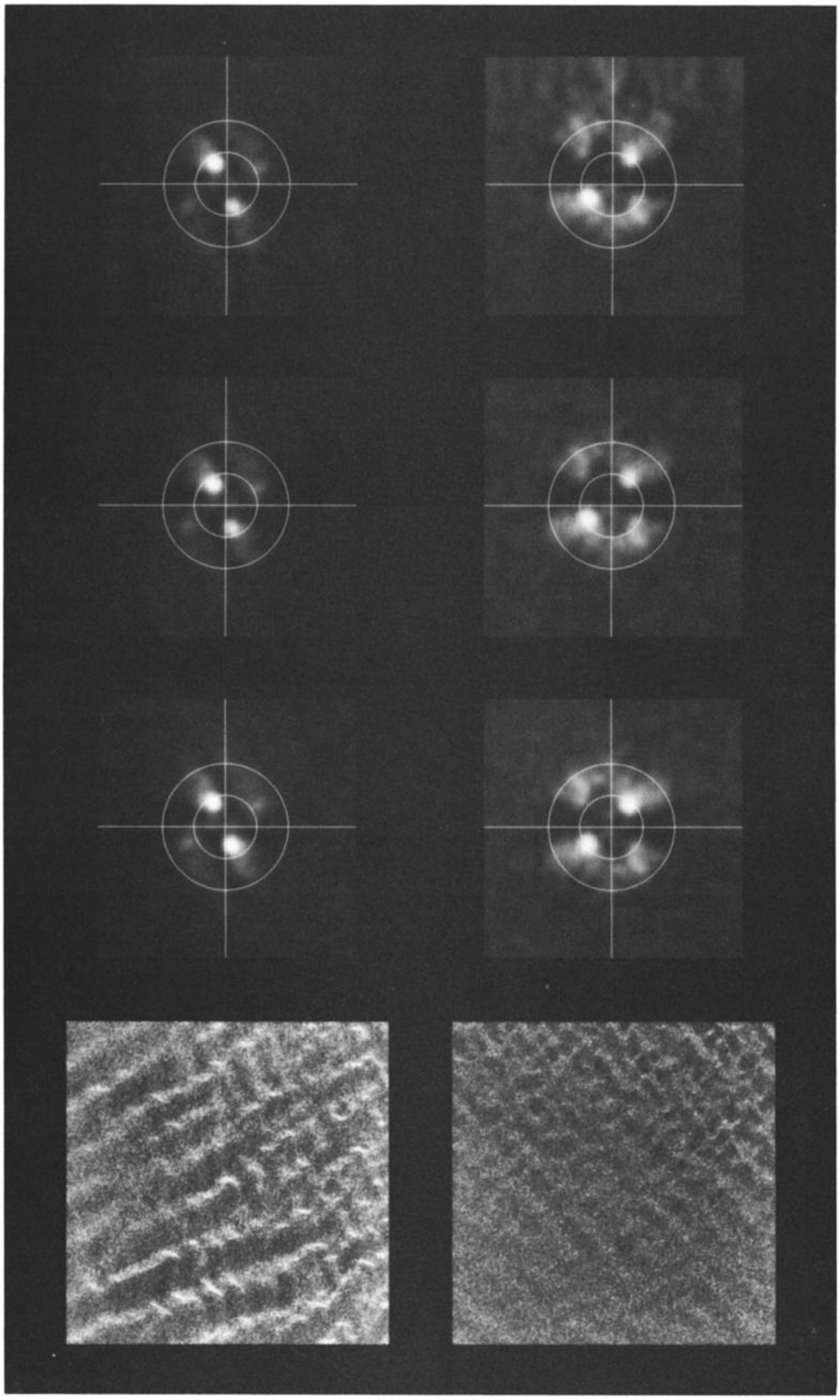

Fig. 7. Representative images and spectral products for the two data collection days considered for wave dispersion. The upper set corresponds to a subscene from March 23 line 7 pass 2 (scene C). The (i) raw spectrum and the scanning corrected spectra with (ii) open water and (iii) wave-in-ice dispersion relation are shown respectively from left to right. The lower set corresponds to a subscene from March 26 line 3 pass 3 (scene E). On the spectra, the outer circle corresponds to 100 m wavelength while the inner circle corresponds to 200 m wavelength.

TABLE 1. Wavelength λ and Propagation Direction θ of the Principal Wave Number Component as a Function of Subscene Range R for the Data From March 23, Line 1, Pass 3

R, km	λ, m	θ, deg
9.2	250 ± 30	240 ± 7
12.6	230 ± 26	240 ± 7
16.2	230 ± 26	220 ± 7
20.0	200 ± 20	220 ± 7
23.9	250 ± 30	220 ± 7

To provide confidence in the approach, the SAR data for peak ocean wavelength from the Labrador Sea Extreme Waves Experiment (LEWEX) and concurrent Wavescan buoy data for peak wave period in the open water [*Vachon et al.*, 1988] were processed similarly. Since the open water dispersion relation is well known, a good model-data comparison for waves in water establishes that confidence. Estimated aircraft SAR response characteristics and ocean wave spectra in LEWEX have been reported by *Tilley* [1989].

In order to assess the ability of the SAR to measure the wave attenuation with penetration into the MIZ, subscenes from the March 23 (line 1, pass 3) and March 26 (line 3, pass 3) SAR image data along swaths with a constant incidence angle have been extracted. From the results measured with the wave spectra, wave attenuation coefficients have been derived which can be compared with those from other sensors and models.

For the March 23 case, the distance of wave penetration into the MIZ was not extensive. Eleven 200 by 200 pixel overlapping subscenes (800 by 800 m) were extracted, each representing an increase of 500 m in wave propagation distances from the ice edge. Representive spectra at distance 1.0, 2.0, 3.0, and 4.0 km are shown in Figure 8*a*, 8*b*, 8*c*, and 8*d* for reference. Note that the waves appear bimodal near the ice edge, but only the dominant wave model persists with increasing distance into the ice pack. Following the notation of *Raney et al.* [1989], the resulting contrast measures are plotted in Figure 9*a* as the log of contrast-squared versus propagation distance for the persistent 230 m wavelength mode. The peak contrast value essentially is a measure of wave amplitude, assuming that velocity bunching is in a linear mapping region. This is a good assumption, as the propagation distance increases and the wave amplitude decreases due to attenuation. Based upon the slope of the least squares fit line, the attenuation coefficient for March 23 is approximately 5.7×10^{-4} m^{-1}. The initially anomalous increase in wave image contrast may be a consequence of velocity bunching nonlinearities, and in particular, of energy from the dominant mode being placed in false spectral components. Given the wave heights measured on this day, the velocity bunching was certainly nonlinear, at least in the vicinity of the ice edge.

For the March 26 case, the waves penetrated into the MIZ from north of Cape St. Francis, propagating southward over much larger spatial distances than were observed on March 23rd. Seventeen overlapping 512 by 512 pixel subscenes (2 by 2 km) were extracted, each representing an increase of about 1.5 km in wave propagation distance from the ice edge. The subscenes were chosen such that the ice conditions were relatively homogeneous along the 34-km swath, the water depth remained consistent with the deep water dispersion relation, and the waves being measured impinged upon the ice edge with a constant incidence angle. The subscenes included ice that had a predominantly uniform gray tone with little variation and do not include the brighter ice nearest the ice edge. On March 26 the uniform ice was compose of small floes separated by unconsolidated brash, with all ice surfaces being wetted due to the air temperatures above 0°C. Any contrast was due primarily to the ice motion on the waves and not to the ice surface variability itself. However, as was mentioned earlier, nearer to the coast the floe size increased, which increased somewhat the variability in the radar return. The resulting contrast measures are plotted in Figure 9*b* for the dominant 320-m wavelength mode. Based upon the least squares fit line, the attenuation coefficient for March 26 is 6.06×10^{-5} m^{-1}. The larger variability in the contrast nearer the coast along this swath is attributed to variability in ice properties, most probably larger floe size, which alters the wave attenuation and dispersion, as a function of spatial position along the rather long swath.

5. MODEL-DATA COMPARISON

Using the SAR imagery, the spatial variability of the dominant wavelength can be estimated through spectral analysis. On the other hand, the wave-induced ice motion

TABLE 2. Average Wavelength λ and Propagation Direction θ for the Primary (First Line) and Secondary (Second Line) Wave Modes as Extracted From the SAR Imagery

	Raw Spectrum		Scanning Corrected $h = 0$ m		Scanning Corrected $h = 1.5$ m	
	λ, m	θ, deg	λ, m	θ, deg	λ, m	θ, deg
L7P2	245	215	221	208	221	208
	149	313	166	309	170	308
L1P3	211	230	233	226	236	226
	140	307	158	310	161	309
L2P4	249	229	230	224	230	224
	141	320	158	315	160	314
L3P3	288	205	334	209	334	209
	176	302	160	305	153	308
L4P4	325	221	287	216	287	216
	141	322	153	319	156	317

Read L7P2 as leg 7, pass 2.

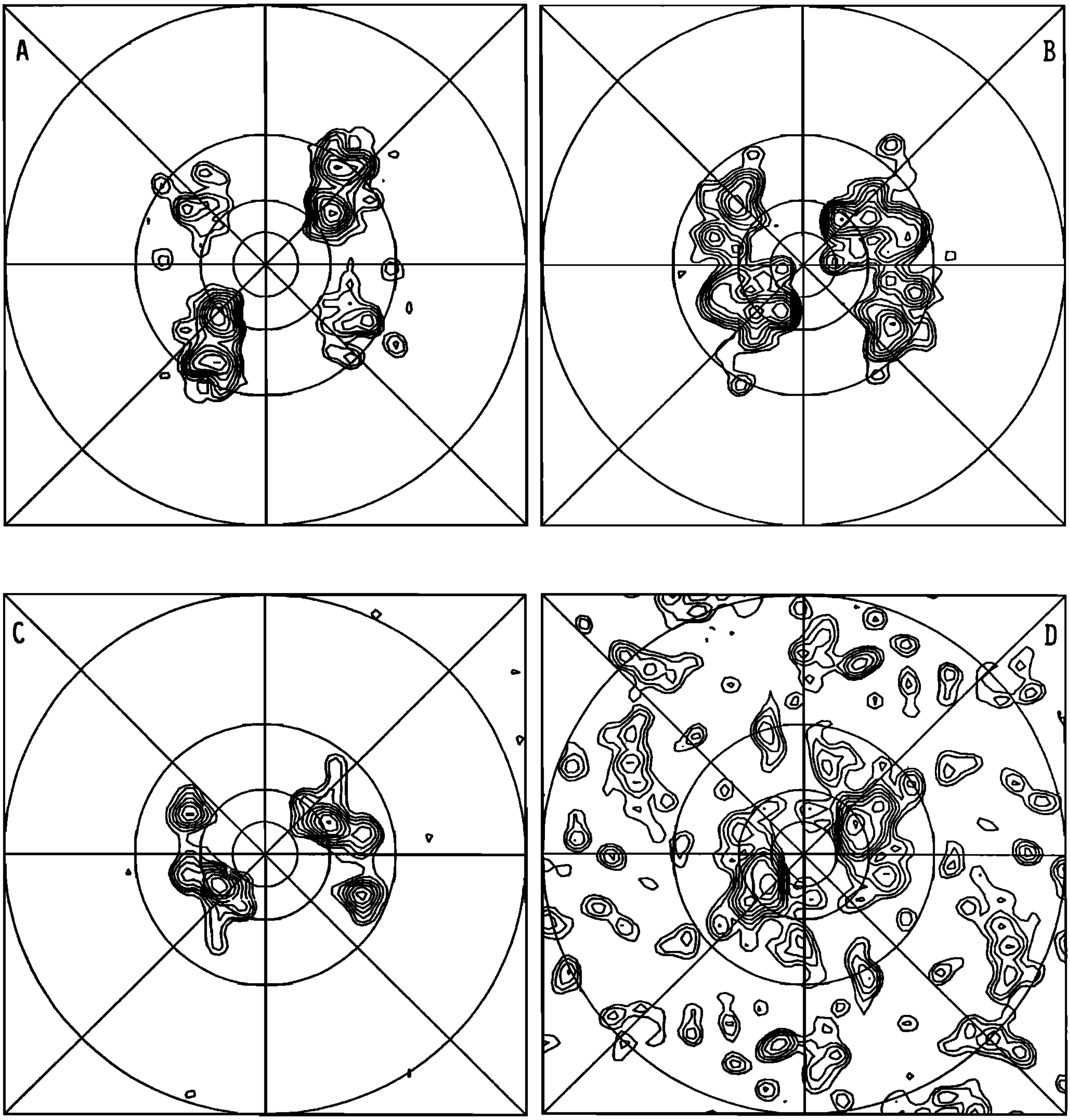

Fig. 8. SAR spectra at (*a*) 1 km, (*b*) 2 km, (*c*) 3 km, and (*d*) 4 km from the ice edge from March 23 (line 1, pass 3).

heave time series or the time history data of the Delft wave buoy collected at nearly the same time as the SAR data allows the dominant wave frequency to be estimated. The error tolerances are based upon an error of one frequency resolution cell in peak location.

To test the approach, the SAR-derived wavelength and Wavescan buoy–derived peak period results during LEWEX in open ocean [*Krogstad*, 1987] are first examined. Figure 10 shows the open water dispersion relation (solid curve) and four data points from LEWEX. The error tolerance in the Wavescan data is 10% of the square of peak value which corresponds to ± -1.4 s [*Allender et al.*, 1991]. As shown in Figure 10, the LEWEX data favorably agree with the open water dispersion relation. In general, the peak wavelength and peak period should follow the dispersion relation as long as the wave spectrum has a narrowly shaped peak, which is especially true for waves in ice owing to the damping of high frequency waves.

Next, the results for waves in ice are related through an appropriate dispersion relation based upon the ice properties (Figure 10). The two dashed curves are model predictions from (1) for the wave dispersion relation in the MIZ with an ice thickness of $h = 1$ m and $h = 2$ m. The average ice thickness during LIMEX '87 was approximately 1.5 m. The dashed curves have also been modified because of the effects of finite water depth at long wave periods. The two LIMEX

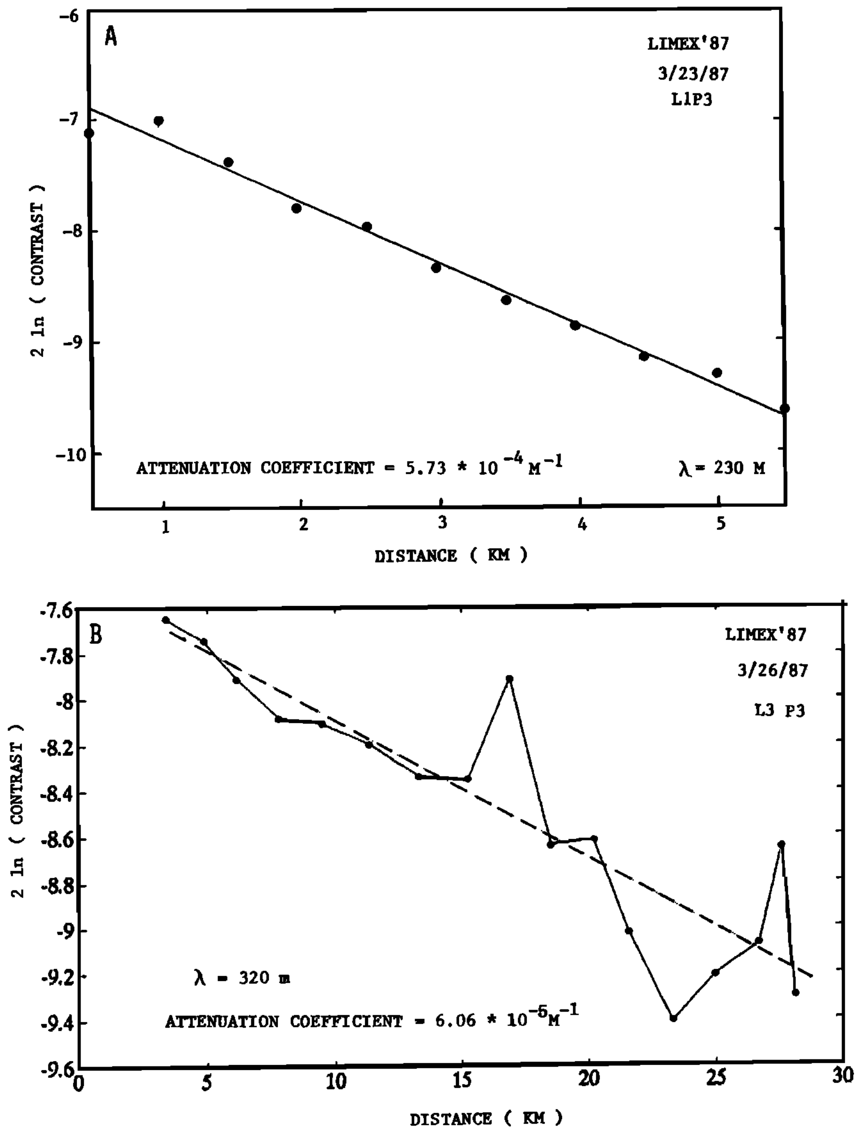

Fig. 9. Logarithm of spectral contrast as a function of the wave propagation distance into the MIZ for a fixed dominant wave mode from (*a*) March 23 and (*b*) March 26. The slope of the solid line is the wave attenuation coefficient.

'87 data sets correspond to the 2 days of SAR data combined with the Delft wave buoy data from March 23 and the ice motion package data from March 26. As shown in Figure 10, the model-data comparison is reasonably good for an ice thickness h of 1–2 m. The error bars correspond to temporal and spatial separation between the SAR and buoy measurement locations and to binning errors in searching for modal locations. For wave periods of less than 14 s, the ice alters the dispersion relation significantly and results in an increase in wavelengths as compared with open water.

The results from the March 25 experiment provide information on the attenuation of waves in ice [*Eid et al.*, 1989]. As was mentioned earlier, one package operated on an ice floe near the ice edge for the duration of the experiment, and a second ice package was deployed at distances of approximately 1, 2, and 4 km into the ice pack. Since the sea state did not change significantly during the course of the experiment on March 25, the measurements collected during different time periods can still be used to test the theory. On the basis of the ice motion package data from March 25, the attenuation of wave energy was estimated by spectral analysis. The attenuation coefficient was calculated for several frequencies (Figure 11). The large error bars for 90% confidence limit at the high frequencies are the result of poor calibration of the accelerometers and very low wave energy at these frequencies. These ice motion package data show that the attenuation of wave energy increases as the frequency increases. However, the large error bars obscure the change of attenuation rate at higher frequencies.

The estimated attenuation coefficients from the spectral contrast of the SAR images on March 23 and March 26 are also shown in Figure 11 as SAR data and are lower than the ice motion package data, but within the error bar for 90% confidence limit. The solid and dashed curves in Figure 11 are the model predictions from (3) for ice thickness h = 1.0 m and h = 1.5 m, respectively. Note that the model compares reasonably well with the ice motion package at lower frequencies but not as well with SAR data and that it predicts a rollover at high wave frequencies, whereby the rapid increase in attenuation coefficient with increasing

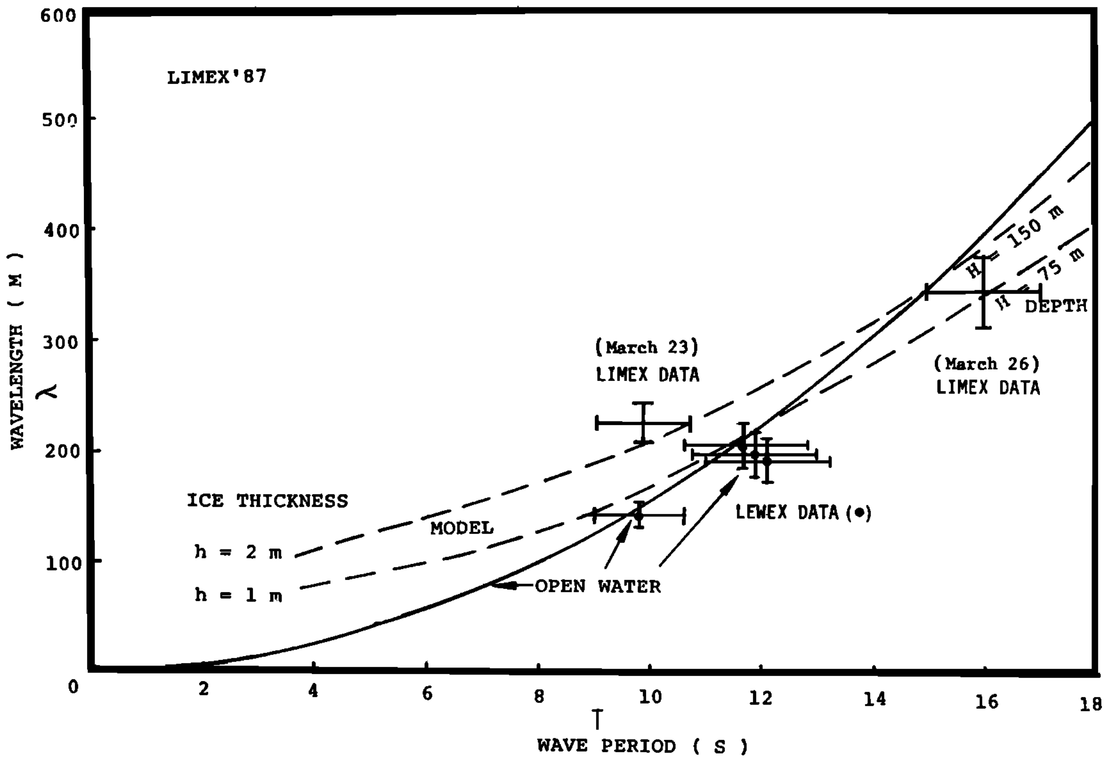

Fig. 10. Model-data comparisons for the wave dispersion relation.

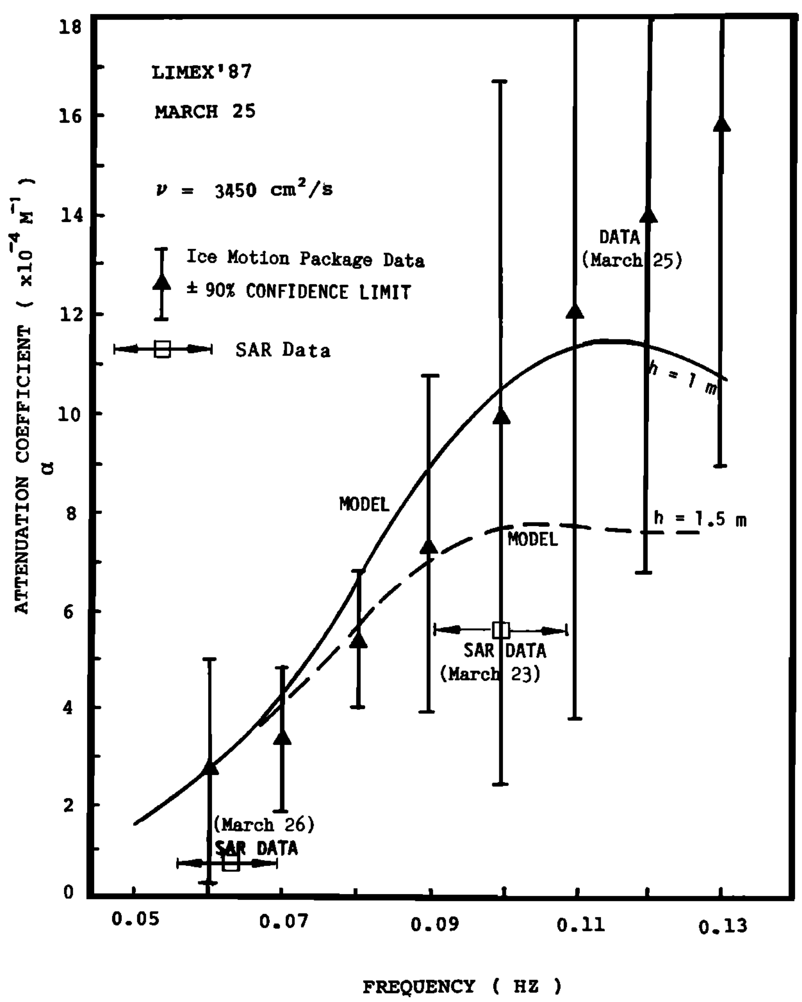

Fig. 11. Model-data comparisons for the wave attenuation coefficient as a function of wave frequency for LIMEX '87.

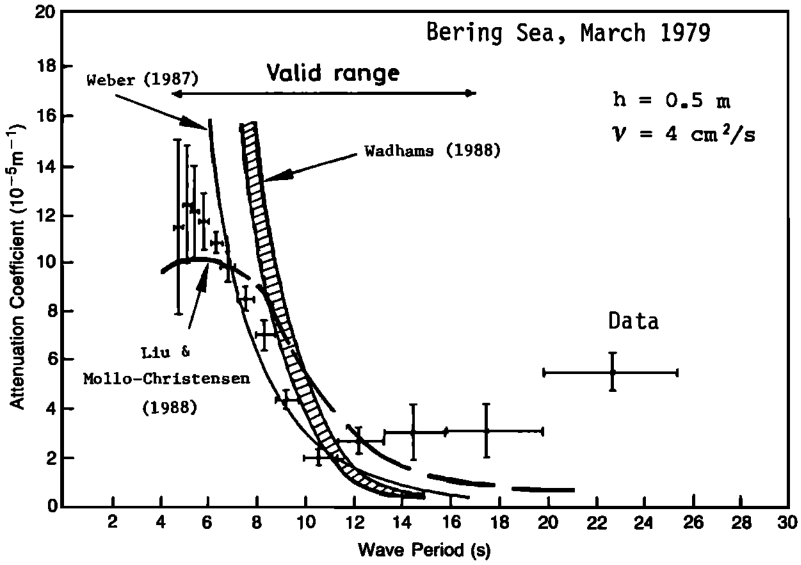

Fig. 12. Model-data comparisons for the wave attenuation coefficient from the Bering Sea in 1979 (data after *Wadhams et al.* [1988]).

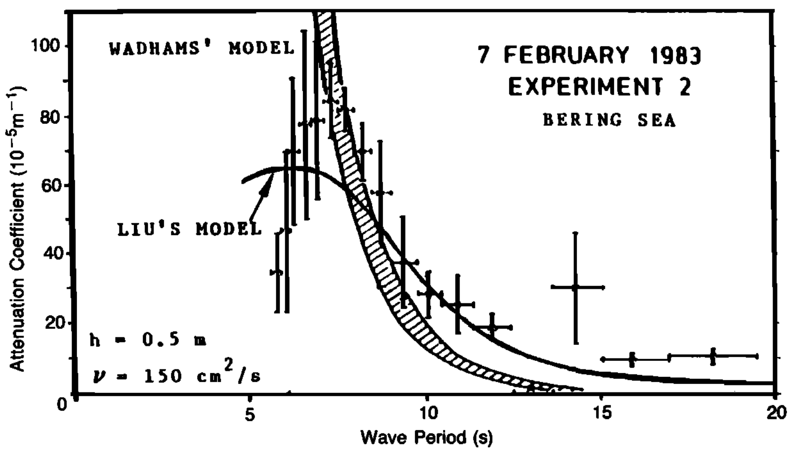

Fig. 13. Wave attenuation coefficient from the Bering Sea on February 7, 1983, for model-data comparison (data after *Wadhams et al.* [1988]).

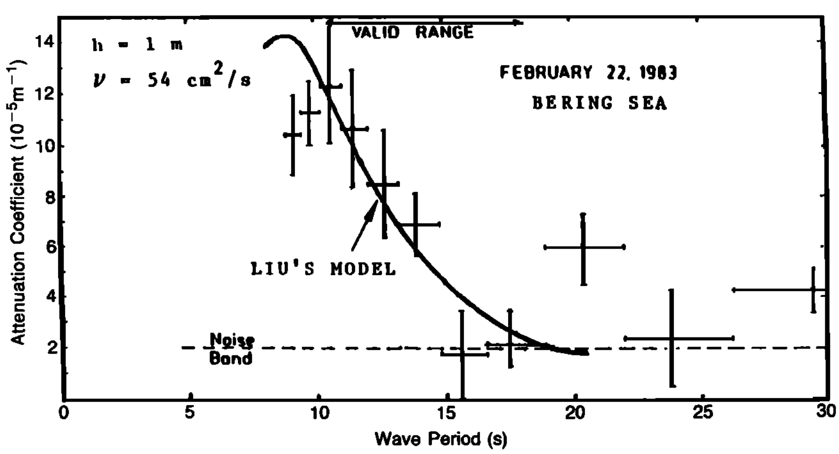

Fig. 14. Wave attenuation coefficient from the Bering Sea on February 22, 1983, for model-data comparison (data after *Wadhams et al.* [1988]).

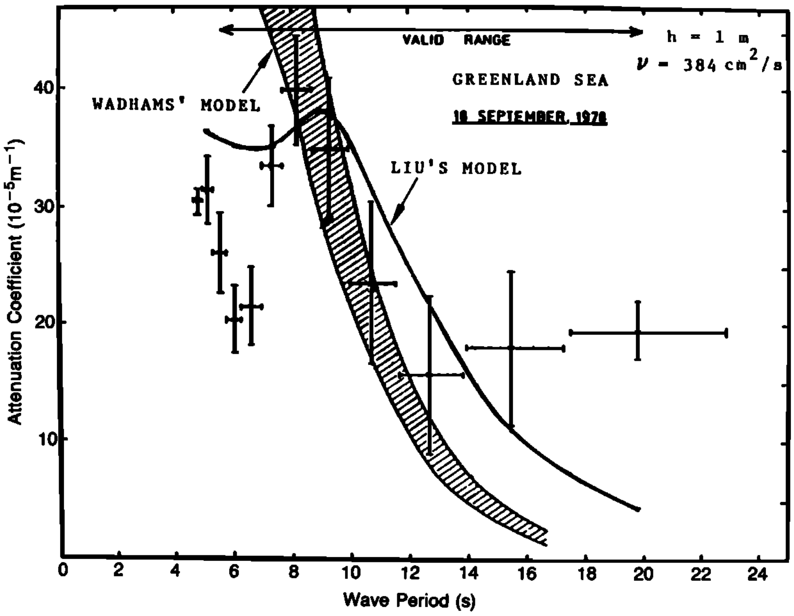

Fig. 15. Wave attenuation coefficient from the Greenland Sea in 1978 for model-data comparison (data after *Wadhams et al.* [1988]).

frequency slows down or even begins to decrease. Basically, in the compact ice fields, the short waves propagate into the ice sheet as flexural gravity waves with altered dispersive properties. The change in wave dispersion due to the ice conditions (e.g., floe size, ice thickness, and ice concentration) is an important problem for wave evolution in the MIZ. As is predicted in the attenuation rate model, the point of rollover depends on ice conditions, especially ice thickness.

In order to further test the model, the previous reported data published by *Wadhams et al.* [1988] were revisited. During field operations in the Greenland and Bering seas in 1978, 1979, and 1983, a number of experiments were carried out in which wave energy was measured by accelerometers along a line of stations from the open sea, deep into the ice field. A detailed description of field experiment and ice conditions is given by *Wadhams et al.* [1988]. They found that the wave attenuation coefficient generally decreases with wave period except for a rollover at the lowest periods. Five of these cases with high ice concentration (larger than 60%) in the MIZ have been selected. A typical case is shown in Figure 12 from the Bering Sea in March 1979. The data on attenuation coefficient α show a rollover at short wave periods T, whereby the rapid increase in α with decreasing T slows down or even turns into a decrease. The wave attenuation models by *Wadhams* [1975] for wave scattering which used the same flexural wave dispersion relation as used here and by *Weber* [1988] for the viscous ice layer which used the open water dispersion relation, do not predict the rollover effect as shown in Figure 12. However, the model developed by *Liu and Mollo-Christensen* [1988] predicts the rollover at short waves and compares reasonably well with the field measurements. For further demonstration and reference, four more cases from the Bering Sea in 1983 and the Greenland Sea in 1978 and 1983 are shown in Figures 13, 14, 15, and 16. Again, the agreement between the model and field data is generally good, and the point at which the rollover occurs depends on ice thickness. The eddy viscosity is the only tuning parameter and is a function of both the flow and ice conditions. The much larger eddy viscosity used in the Greenland Sea is due to high turbulent level in the MIZ which consists mainly of multiyear ice. The smaller eddy viscosity used in the Bering Sea corresponds to relatively young ice.

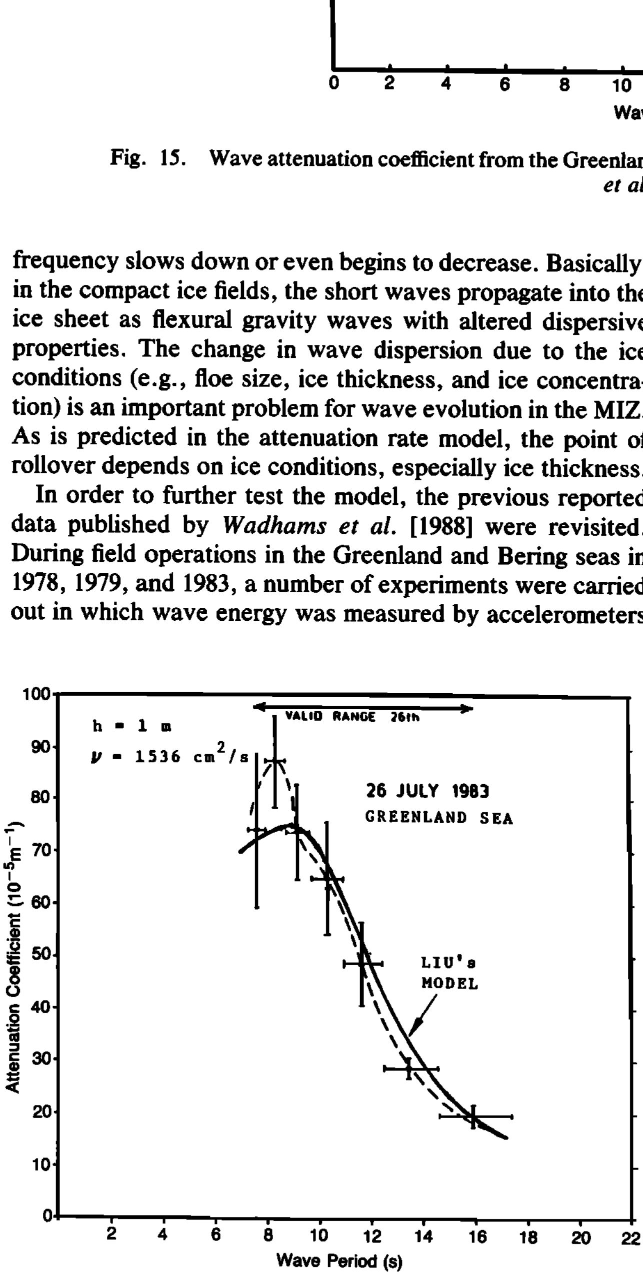

Fig. 16. Wave attenuation coefficient from the Greenland Sea in 1983 for model-data comparison (data after *Wadhams et al.* [1988]).

6. DISCUSSION

In this paper the effects of an ice cover on the ocean wave dispersion relation and wave attenuation are studied for waves under flexure in the MIZ. As predicted by the simple elastic ice sheet model, the flexure effect is important for short waves. By using this model with ice thickness as the major parameter for ice condition, a procedure to extract wave and ice parameters from buoy and SAR data has been developed. LIMEX '87 provides SAR, buoy, and ice property data. This diverse and nearly complete data set presents an opportunity to study the dispersion and attenuation of ocean waves penetrating the MIZ.

Based on the wave number spectrum from SAR data and the concurrent wave frequency spectrum from buoy and accelerometer data during LIMEX '87, the dispersion relation has been derived and compared with a model. As a test case, open water LEWEX '87 wave data are used and agree well with the open water dispersion relation, which provides encouragement for use of the procedure, especially for a narrowly peaked waves-in-ice spectrum. Wave attenuation rates are estimated from peak contrast calculations of SAR subscenes along a swath into the ice pack. Wave attenuation was also studied using a series of measurements made with several wave accelerometers during LIMEX '87 and compared with the model.

The model-data comparisons are reasonably good for the ice and wave conditions during LIMEX '87. However, there are only two data sets, from March 23 and 26, available with both SAR and buoy measurements for examining the waves in ice dispersion relation. During LIMEX '87, the ice cover was heavily compacted and rafted because of the easterly wind. Although the individual floes are distinguishable, they are connected by brash ice frozen together and are not completely free. It is evident that the effect of the ice cover is significant for short waves. This elastic model of continuous ice sheet should be considered as a first-order correction to the open water model. For length scales of longer than 100 m waves, the small cracks between ice floes are neglected. In the MIZ the ice cover is definitely not a perfect elastic plate. An "effective Young's modulus" may be used for a better fit to the data. Extensions to a higher-order plastic model will involve more tuning parameters and can be tested when more data sets are available. The model-data comparison shows that the first-order elastic model of a continuous ice sheet has the right trend in correcting the open water case. Further study is underway for LIMEX '89 using the four CV-580 SAR flights which were dedicated to waves-in-ice studies.

The wave attenuation model predicts a rollover at short wave periods, whereby the rapid increase in the wave attenuation coefficient with decreasing wave period slows down or even shows a decrease. The model predictions agree well with Wadhams' data from a series of field experiments carried out between 1978 and 1983 in the Greenland and Bering seas. As is predicted in the viscous boundary layer model, the point of rollover in wave attenuation coefficient depends on ice conditions, especially ice thickness. The only tuning parameter is the turbulent eddy viscosity, and it is a function of the flow conditions in the turbulent boundary layer which are determined by the ice thickness, floe sizes, ice concentration, and wavelength. Since the eddy viscosity is not a physical property of the fluid but rather a dynamic property of the specific flow, the constant values used may not be very representative and may vary significantly because of different ice conditions in different MIZ regions. However, the use of eddy viscosity often gives at least a qualitatively sensible picture of those aspects of large-scale dynamics of ocean-ice interaction. Dimensional analysis can sort out the parametric dependence, but more data are required to more quantitatively evaluate the final model for eddy viscosity. It is demonstrated that we can extract some wave and ice parameters from SAR imagery and buoy data coupled with the waves-in-ice model in the MIZ.

Acknowledgments. The authors wish to thank the LIMEX/LEWEX '87 experimental teams for coordinating and collecting the data set used in this work. The ice motion package data were supplied by B. Eid of MacLaren Plansearch. The Delft buoy data were supplied by W. Thomas of David Taylor Research Center. The authors would also like to acknowledge many valuable suggestions and the numerical assistance of A.S. Bhogal and C.Y. Peng. The GSFC work was supported by the National Aeronautics and Space Administration and Office of Naval Research. The JPL participation was performed by the Jet Propulsion Laboratory, California Institute of Technology, under contract to the National Aeronautics and Space Administration.

REFERENCES

Allender, J., T. Audunson, S. F. Barstow, S. Bjerken, H. E. Krogstad, P. Steinbakke, L. Vartdal, L. E. Borgman, and C. Graham, The WADIC project: A comprehensive field evaluation of directional wave instrumentation, *Ocean Eng.*, in press, 1991.

Brennecke, B., Die ozeanographischen Arbeiten der Deutschen Antarktischen Expedition 1911–1912, *Arch. Dtsch. Seewarte, 39*, 206, 1921.

Carsey, F. D., S. A. Digby Argus, M. J. Collins, B. Holt, C. E. Livingstone, and C. L. Tang, Overview of LIMEX '87 ice observations, *IEEE Trans. Geosci. Remote Sens.*, *27*, 468–482, 1989.

Dawe, B. R., and S. K. Parashar, SAR imageing of waves in ice, *Oceans '78*, pp. 379–384, Mar. Technol. Soc., Washington, D. C., 1978.

Drinkwater, M. R., LIMEX '87 ice surface characteristics: Implications for *C*-band SAR backscatter signatures, *IEEE Trans. Geosci. Remote Sens.*, *27*, 501–513, 1989.

Drinkwater, M. R., and V. A. Squire, *C*-band SAR observations of marginal ice zone rheology in the Labrador Sea, *IEEE Trans. Geosci. Remote Sens.*, *27*, 522–534, 1989.

Eid, B. M., C. M. Morton, W. D. Windsor, and V. J. Cardone, Wave-ice interaction study during LIMEX '87, paper presented at 2nd International Workshop on Wave Hindcasting and Forecasting, Atmos. Environ. Serv., Environ. Can., Vancouver, B. C., April 1989.

Hunkins, K., Ekman drift current in the Arctic Ocean, *Deep Sea Res.*, *13*, 607–620, 1986.

Krogstad, H. E., Wave data collected by Wavescan during the Labrador Sea Extreme Waves Experiment (LEWEX), *Rep. 87.111*, Oceanogr. Center, SINTEF, Trondheim, Norway, 1987.

Liu, A. K., and E. Mollo-Christensen, Wave propagation in a solid ice pack, *J. Phys. Oceanogr.*, *18*, 1720–1712, 1988.

Livingstone, C. E., A. L. Gray, R. K. Hawkins, R. B. Olsen, R. A. Deane, and J. G. Halbertsma, CCRS *C*-band airborne radar-system description and test results, paper presented at 11th Canadian Symposium on Remote Sensing, Can. Centre for Remote Sens., Waterloo, Ont., June 1987.

Lyzenga, D. R., R. A. Shuchman, L. D. Lyden, and C. L. Rufenach, SAR imaging of waves in water and ice: Evidence for velocity bunching, *J. Geophys. Res.*, *90*, 1031–1036, 1985.

Martin, S., and P. Kauffman, A field and laboratory study of wave damping by grease ice, *J. Glaciol.*, *27*, 283–313, 1981.

Masson, D., and P. H. LeBlond, Spectral evolution of wind-generated surface gravity waves in a dispersed ice field, *J. Fluid Mech.*, *202*, 43–81, 1989.

Raney, R. K., Wave orbital velocity, fade, and SAR response to azimuth waves, *IEEE J. Oceanic Eng.*, *OE-6*, 140–146, 1981.

Raney, R. K., and P. W. Vachon, Synthetic aperture radar imaging of ocean waves from an airborne platform: Focus and tracking issues, *J. Geophys. Res.*, *93*, 12,475–12,486, 1988*a*.

Raney, R. K., and P. W. Vachon, SAR-seen multi-mode waves in ice: Evidence of imaging nonlinearities, paper presented at International Geoscience and Remote Sensing Symposium (IGARSS '88), IEEE, Edinburgh, Scotland, Sept. 1988*b*.

Raney, R. K., P. W. Vachon, R. A. DeAbreu, and A. S. Bhogal, Airborne SAR observations of ocean surface waves penetrating floating ice, *IEEE Trans. Geosci. Remote Sens.*, *27*, 492–500, 1989.

Shen, H. H., W. D. Hibler, and M. Leppäranta, The role of floe collisions in sea-ice rheology, *J. Geophys. Res.*, *92*, 7085–7096, 1987.

Squire, V. A., A theoretical, laboratory, and field study of ice-coupled waves, *J. Geophys. Res.*, *89*, 8069–8079, 1984.

Squire, V. A., and A. J. Allan, Propagation of flexural gravity waves in sea ice, in *Proceedings of the AIDJEX/ICSI Symposium*, edited by R. S. Pritchard, pp. 327–338, University of Washington Press, Seattle, 1980.

Thomas, W. L., Labrador Sea wave and ice measurements in support the March 1987 LIMEX, *Rep. DTRC/SHD-1212-05*, 29 pp., David W. Taylor Res. Center, Bethesda, Md., June 1988.

Tilley, D. G., Estimating aircraft SAR response characteristics and ocean wave spectra in the Labrador Sea Extreme Waves Experiment, *IEEE Trans. Geosci. Remote Sens.*, *27*, 483–491, 1989.

Vachon, P. W., R. B. Olsen, C. E. Livingstone, and N. G. Freeman, Airborne SAR imagery of ocean surface waves obtained during LEWEX: Some initial results, *IEEE Trans. Geosci. Remote Sens.*, *26*, 548–561, 1988.

Wadhams, P., Attenuation of swell by sea ice, *J. Geophys. Res.*, *78*, 3552–3563, 1973.

Wadhams, P., Airborne laser profiling of swell in an open ice field, *J. Geophys. Res.*, *80*, 4520–4528, 1975.

Wadhams, P., The seasonal ice zone, in *The Geophysics of Sea Ice*, edited by N. Untersteiner, pp. 825–991, Plenum, New York, 1986.

Wadhams, P., V. A. Squire, J. A. Ewing, and R. W. Pascal, The effect of the marginal ice zone on the directional wave spectrum of the ocean, *J. Phys. Oceanogr.*, *16*, 358–376, 1986.

Wadhams, P., V. A. Squire, D. J. Goodman, A. M. Cowan, and S. C. Moore, The attenuation rates of ocean waves in the marginal ice zone, *J. Geophys. Res.*, *93*, 6799–6818, 1988.

Weber, J. E., Wave attenuation and wave drift in the marginal ice zone, *J. Phys. Oceanogr.*, *17*, 2351–2361, 1987.

B. Holt, Jet Propulsion Laboratory, California Institute of Technology, 4800 Oak Grove Drive, Pasadena, CA 91109.

A. K. Liu, Oceans and Ice Branch, NASA Goddard Space Flight Center, Greenbelt, MD 20771.

P. W. Vachon, Canada Centre for Remote Sensing, 2464 Sheffield Road, Ottawa, Ontario, Canada KIA 0Y7.

(Received March 28, 1990;
revised September 17, 1990;
accepted July 16, 1990.)